JOURNAL OF APPLIED PHYSICS **102**, 093103 (2007)

Design of *n*-type silicon-based quantum cascade lasers for terahertz light emission

Kristina Driscoll and Roberto Paiella[a]
Department of Electrical and Computer Engineering and Photonics Center Boston University, Boston, Massachusetts 02215, USA and Photonics Center, Boston University, Boston, Massachusetts 02215, USA

(Received 6 August 2007; accepted 10 September 2007; published online 6 November 2007)

The design of terahertz quantum cascade lasers based on electronic intersubband transitions in Ge/SiGe quantum wells is investigated. A detailed theoretical model of the conduction-band lineup of these heterostructures is first presented and used to show that large quantum confinement in the *L* valleys can be obtained with properly selected layer compositions and thicknesses. Computation of the key laser design parameters is then discussed, including the important role played by the *L*-valley ellipsoidal constant-energy surfaces. Finally, the main design issues specific to this material system and its potential for high-performance operation are illustrated by means of two exemplary structures, designed for emission near 50 and 25 μm. © *2007 American Institute of Physics*.
[DOI: 10.1063/1.2803896]

I. INTRODUCTION

The terahertz region of the electromagnetic spectrum has so far remained relatively unexplored mainly due to the lack of practical sources and detectors. Sitting between the traditional domains of electronics and photonics, technological development in this spectral range has been slow as conventional devices from either domain often cannot be readily extended to operate at terahertz frequencies. Yet, the potential of terahertz radiation in numerous applications, including medical diagnostics, security screening, and manufacturing quality control, has recently been identified and is driving efforts to develop the required system components.[1] A promising approach for the realization of terahertz semiconductor lasers is the use of intersubband (ISB) transitions in the quantum cascade (QC) scheme. In this lasing modality, the emission wavelength is not directly dependent on the band gap of the constituent materials and is tunable through the design of the layer thicknesses in the multiple-quantum-well (QW) active material.

Recently the extension of this principle to the terahertz frequency range has been demonstrated with GaAs/AlGaAs heterostructures.[2–5] However, the operation of these devices is limited by an intrinsic property of AlGaAs, namely, the presence of polar optical phonons with frequencies in the terahertz region. As a result AlGaAs terahertz QC lasers are completely precluded from emission near their reststrahlen band in the 30–40 μm range. Additionally, the population inversion in these devices is rapidly degraded with increasing temperature by fast nonradiative transitions between the laser subbands due to thermally activated LO phonon emission; consequently their operation is limited to cryogenic temperatures. Therefore, the search for novel semiconductor systems capable of extending both the wavelength range and the operating temperature of terahertz injection lasers remains an important endeavor.

One such promising material system is SiGe which, due to its nonpolar nature, is free from reststrahlen absorption and from resonant electron-phonon scattering, and thus is potentially capable of high-temperature high-performance operation over a wide wavelength range. It should also be noted that the demonstration of electrically pumped silicon lasers is a highly sought-after goal in itself, as it would enable fully monolithic wafer-scale integration of photonic and electronic components. While research in this area has long been complicated by the indirect band gap of silicon, the use of QC lasers circumvents this issue as ISB transitions involve quantized states within the same energy band. In fact, following a number of theoretical proposals,[6,7] a few groups have recently reported ISB electroluminescence from SiGe QC structures at mid- and far-infrared wavelengths,[8–10] but lasing has yet to be observed.

Thus far, nearly all efforts in developing Si-based ISB devices have made use of hole ISB transitions, motivated by the generally less favorable properties of the QWs in the conduction band compared to those in the valence bands of SiGe heterostructures. Specifically,[11] a compressively strained $Si_{1-x}Ge_x$ well layer grown pseudomorphically on a $Si_{1-y}Ge_y$ substrate (with $y<x$) results in a negligibly small overall conduction-band offset ΔE_c (a few tens of meV). Tensile strained SiGe wells can provide larger ΔE_c; however, their conduction-band minima occur in the two Δ valleys along the growth direction ($\Delta 2$), whose large perpendicular effective masses ($\sim 0.9 m_0$) lead to exceedingly small ISB oscillator strengths and reduced interwell tunneling rates. On the other hand, the design of hole ISB devices is complicated by the intricacy of the valence-band structure. In particular, it is difficult to achieve population inversion in these devices as the presence of heavy-hole and mixed light-hole/split-off subbands at comparable energies results in strong nonradiative decay paths from the upper laser states.[12]

In a recent letter,[13] we have introduced an alternative ISB approach that avoids the complexities of the valence bands, and we have presented an exemplary QC gain-medium design for emission near 40 μm as an illustration.

[a]Electronic mail: rpaiella@bu.edu

 © 2007 American Institute of Physics

Downloaded 06 Nov 2007 to 128.197.173.60. Redistribution subject to AIP license or copyright, see http://jap.aip.org/jap/copyright.jsp

This approach relies on electronic ISB transitions in the L valleys of $Ge/Si_{1-x}Ge_x$ QWs pseudomorphically grown on $Si_{1-y}Ge_y$ (001) virtual substrates with $y>x$. In these heterostructures, if sufficiently thin $Si_{1-x}Ge_x$ barriers are used, a substantial quantum confinement is obtained for the L-valley electrons despite a small overall conduction-band offset ΔE_c. At the same time, the L valleys provide particularly small electronic effective masses along the (001) growth direction, as well as nonzero off-diagonal terms of the inverse effective-mass tensor. The latter feature is also advantageous as it enables surface-normal ISB light emission, which may be used to overcome the low outcoupling efficiency and large beam divergence of existing in-plane terahertz QC lasers based on plasmon waveguides. In addition, the fourfold degeneracy of the L valleys results in a larger density of states of the laser subbands (for fixed effective mass), which can be expected to improve the device capability to conduct large current densities and hence emit high output power.

The purpose of this work is to provide a comprehensive description of how this promising class of far-infrared QC lasers can be designed. In Sec. II we present the theoretical model used to compute the conduction-band lineups of the L and Δ valleys, and using this model we discuss how the template and barrier compositions can be selected to maximize the electronic quantum confinement in n-type Ge/SiGe QC structures. Section III is devoted to the calculation of the bound-state energies and envelope functions of these structures and of the related key laser design parameters such as oscillator strengths and phonon-assisted ISB scattering lifetimes. In particular, the role of the nondiagonal inverse effective-mass tensor of the L valleys is highlighted in this discussion. Finally, in Sec. IV we apply this model to design two structures for emission near 50 and 25 μm, i.e., roughly spanning the spectral gap left uncovered by III-V materials. Design considerations specific to the Ge/SiGe QW system, related to the nonpolar nature of electron-phonon interactions and to the presence of parasitic $\Delta 2$ states, are also discussed in this section, as well as possible approaches to reduce the shortest achievable emission wavelengths. The main conclusions of this study are then summarized in Sec. V.

II. CONDUCTION-BAND LINEUPS

The ability to obtain strong quantum confinement in the L valleys of SiGe heterostructures is suggested by the large increase in the L energy minimum with decreasing Ge content (relative to both the valence band edges and the Δ minimum) measured in these materials.[14,15] The detailed band lineups depend on the chemical composition of the layers involved as well as on their state of strain, which in turn is determined by the substrate composition. The QC lasers described in this work consist of alternating compressively strained Ge wells and tensile strained $Si_{1-x}Ge_x$ barriers grown on $Si_{1-y}Ge_y$ (001) virtual substrates with $y>x$. To compute the resulting conduction-band offsets we use the model-solid theory developed in Ref. 16 in which the average energy of the three valence-band maxima $E_{v,\mathrm{avg}}$ is taken as a reference from which the conduction band minima of

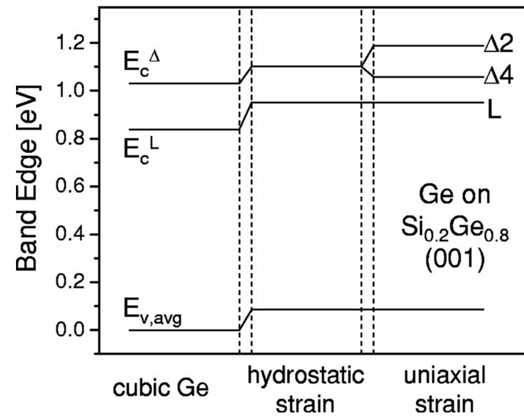

FIG. 1. Contributions of hydrostatic and uniaxial strain to the band-edge energies of a Ge layer pseudomorphically grown on a $Si_{0.2}Ge_{0.8}$ (001) substrate.

the L and Δ valleys $E_c{}^{L,\Delta}$ are calculated. Specifically, for the general case of a strained $Si_{1-x}Ge_x$ layer on a $Si_{1-y}Ge_y$ substrate,

$$E_c{}^{L,\Delta}(x,y) = E_{v,\mathrm{avg}}(x,y) + \frac{1}{3}\Delta_0(x) + E_g{}^{L,\Delta}(x) + E_h{}^{L,\Delta}(x,y) + E_u{}^{L,\Delta}(x,y), \quad (1)$$

where $E_g{}^{L,\Delta}$ and Δ_0 are the unstrained Γ-(L,Δ) bandgaps and spin-orbit splitting of bulk SiGe, respectively, $E_h{}^{L,\Delta}$ is the compositionally dependent bandgap shift due to hydrostatic strain, and $E_u{}^{L,\Delta}$ is the contribution of uniaxial strain. In QWs grown along the (001) direction, the latter term leads to a splitting of the sixfold degenerate Δ valleys into four equivalent in-plane valleys ($\Delta 4$) and two equivalent valleys along the growth direction ($\Delta 2$). On the other hand, no such splitting occurs in the eightfold degenerate L valleys, i.e., $E_u{}^L \equiv 0$, due to their symmetric orientation about (001). The role played by the various terms of Eq. (1) is illustrated schematically in Fig. 1.

This model is based on the observation that the average valence-band edge $E_{v,\mathrm{avg}}$ depends weakly and in a linear fashion on strain and therefore can be taken as a convenient intrinsic parameter to describe the SiGe heterojunction. This observation has emerged from a number of theoretical studies based on *ab initio* or empirical pseudopotentials,[16–18] and has also been confirmed experimentally.[19,20] In this work we use a widely accepted interpolation formula for $E_{v,\mathrm{avg}}$ versus substrate and strained-layer Ge contents y and x, which has been suggested in Ref. 18 in agreement with the data of Ref. 19:

$$E_{v,\mathrm{avg}} = (0.47 - 0.06y)(x-y) \text{ eV}. \quad (2)$$

The unstrained bandgaps $E_g{}^{L,\Delta}$ are calculated with the following expressions, fitted from experimental data in Ref. 15:

$$E_g{}^L = 2.01 - 1.27x \text{ eV},$$
$$E_g{}^\Delta = 1.155 - 0.43x + 0.206x^2 \text{ eV}. \quad (3)$$

Finally, the last two terms in Eq. (1) can be written as[16]

Downloaded 06 Nov 2007 to 128.197.173.60. Redistribution subject to AIP license or copyright, see http://jap.aip.org/jap/copyright.jsp

TABLE I. Summary of the material parameters used in the calculation of the conduction-band edges at the L and Δ points.

	Silicon	Germanium
a [Å]	5.431	5.657
C_{11} [10^6 N cm^{-2}]	16.75	13.15
C_{12} [10^6 N cm^{-2}]	6.5	4.94
Δ_0 [meV]	44	296
$a_c^{L}-a_v$ [eV]	−3.12	−2.78
$a_c^{\Delta}-a_v$ [eV]	1.72	1.31
Ξ_u^{Δ} [eV]	9.16	9.42

$$E_h^{L,\Delta} = (a_c^{L,\Delta} - a_v)(2\varepsilon_{\parallel} + \varepsilon_{\perp}), \tag{4}$$

and

$$E_u^{\Delta} = \begin{cases} \frac{2}{3}\Xi_u^{\Delta}(\varepsilon_{\perp} - \varepsilon_{\parallel}), & \text{for } \Delta_2 \\ -\frac{1}{3}\Xi_u^{\Delta}(\varepsilon_{\perp} - \varepsilon_{\parallel}), & \text{for } \Delta_4, \end{cases} \tag{5}$$

where the strain components parallel and perpendicular to the interface ($\varepsilon_{\parallel}$ and $\varepsilon_{\perp}$) depend on the in-plane lattice constants of the unstrained substrate and adlayer materials (a_{sub} and a_{lay}) as follows:

$$\varepsilon_{\parallel} = \frac{a_{\text{sub}}}{a_{\text{lay}}} - 1, \qquad \varepsilon_{\perp} = -2\frac{C_{12}}{C_{11}}\varepsilon_{\parallel}. \tag{6}$$

All the parameters required to evaluate Eq. (1) numerically, including the unstrained lattice constants, the deformation potentials $a_c^{L,\Delta}$, a_v, and Ξ_u^{Δ}, the elastic constants C_{11} and C_{12}, and the spin-orbit splitting Δ_0, are computed using linear fits to the Si and Ge values listed in Table I. These values can be found, e.g., in two recent review articles on SiGe heterostructures.[11,21]

In Fig. 2 we plot the calculated conduction-band edges of the L, $\Delta 2$, and $\Delta 4$ valleys of a strained $Si_{1-x}Ge_x$ layer on a $Si_{1-y}Ge_y$ substrate versus x for $y=0.8$ (dotted lines), 0.9 (dashed lines), and 1 (solid lines). For each substrate composition, these curves were shifted so that the zero of energy coincides with the L-valley minimum in pure Ge ($x=1$). According to these results, $Ge/Si_{1-x}Ge_x$ QWs can be readily designed with relatively large band offsets in the L valleys ΔE_c^{L}, e.g., comparable to the overall conduction-band offsets in AlGaAs terahertz QC lasers which are typically about 130 meV.[2–5] However, as the barrier Ge concentration x is decreased to increase ΔE_c^{L} the $\Delta 2$ and $\Delta 4$ minima are pushed to lower energies, ultimately limiting the overall conduction-band offset ΔE_c (i.e., the energy separation between the absolute conduction-band minima in the $Si_{1-x}Ge_x$ and Ge layers) to values smaller than ΔE_c^{L}. The resulting conduction-band lineups of such $Ge/Si_{1-x}Ge_x$ heterostructures consist of L-valley and $\Delta 2(4)$-valley QWs inverted relative to one another. An example is shown in Fig. 3 where the solid, dashed, and dotted lines correspond to the L, $\Delta 2$, and $\Delta 4$ valleys, respectively, for the case of $x=0.78$ and $y=0.88$.

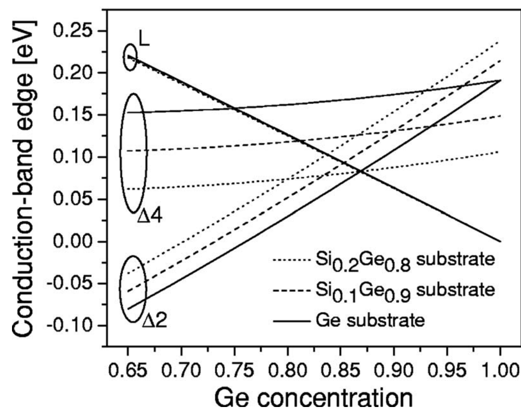

FIG. 2. Conduction-band minima of the L, $\Delta 2$, and $\Delta 4$ valleys of a $Si_{1-x}Ge_x$ layer pseudomorphically grown on a $Si_{1-y}Ge_y$ (001) substrate vs x, for $y=0.8$ (dotted), 0.9 (dashed), and 1 (solid).

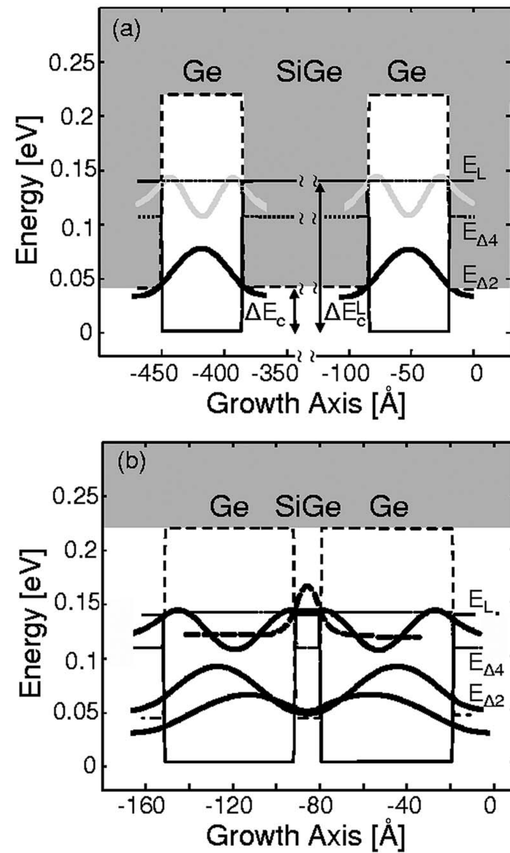

FIG. 3. Conduction-band lineup and squared envelope functions of the relevant bound states of $Ge/Si_{0.22}Ge_{0.78}$ QWs on a $Si_{0.12}Ge_{0.88}$ (001) substrate with (a) wide and (b) narrow barriers. The solid, dashed, and dotted lines correspond to the L, $\Delta 2$, and $\Delta 4$ valleys, respectively. In (a) the light gray solid lines represent L-valley bound states which are extremely short lived due to intervalley scattering into the shaded $\Delta 2$ quasicontinuum.

As illustrated in this figure, the degree of quantum confinement for the L-valley electrons in the Ge wells strongly depends on the available Δ-valley states in the adjacent $Si_{1-x}Ge_x$ layers. In particular, if these layers are thick on the scale of the electronic de Broglie wavelength as in the example of Fig. 3(a), they support a quasicontinuum of $\Delta 2$ states extending down to the local conduction-band mini-

Downloaded 06 Nov 2007 to 128.197.173.60. Redistribution subject to AIP license or copyright, see http://jap.aip.org/jap/copyright.jsp

mum (as indicated by the shaded area in the figure). In this case the excited L states in the Ge wells are very short lived due to fast intervalley scattering processes, and for all practical purposes quantum confinement in these wells is only provided by the small overall conduction-band offset ΔE_c. In QC lasers, however, very thin barriers are commonly used to allow for interwell tunneling, leading to the situation depicted schematically in Fig. 3(b). In this case the lowest $\Delta 2$ bound state in each $Si_{1-x}Ge_x$ barrier (also shown in the figure) lies at a relatively high energy above the band edge due to quantum-size effects, and as a result the L-valley electrons in the Ge wells are confined over an energy range much larger than ΔE_c.

From the results plotted in Figs. 2 and 3 and similar simulations, it follows that the material system used in this example [i.e., Ge/$Si_{0.22}Ge_{0.78}$ QWs on a $Si_{0.12}Ge_{0.88}$ (001) template] provides a favorable compromise between the two key band offsets $\Delta E_c{}^L$ and ΔE_c, which are computed to be 138 and 41 meV, respectively. At the same time, the $\Delta 4$ band edges in both Ge and $Si_{0.22}Ge_{0.78}$ layers lie at sufficiently high energies that they do not affect the electronic confinement in the L-valley QWs. Incidentally it should be noted that the requirement of energetically high $\Delta 4$ valleys effectively limits the smallest substrate Ge concentration suitable for this application, as can be seen from Fig. 2. Finally the Γ edge lies at even higher energy and thus can be fully neglected. Based on these considerations, the material choice of Fig. 3 can be argued to be nearly optimal with regards to electronic quantum confinement in the L valleys and thus has been selected for the design of the far-infrared QC lasers described below.

This QW system also provides strain compensation and can be grown on the standard Si(001) substrates of microelectronics thanks to the availability of high quality SiGe virtual substrates on Si(001).[11] In fact, similar Ge/SiGe QWs have been reported recently as promising candidates for novel optoelectronic applications of silicon, such as the quantum-confined Stark effect.[22,23] Finally it should be pointed out that several band-lineup calculations of SiGe heterostructures have been presented in the literature (ranging from microscopic studies based on pseudopotentials[16,18] or tight-binding methods[24] to variations of the model-solid theory[11,21,25]), whose predictions exhibit some discrepancies with one another. However, they all suggest that conduction-band offsets suitable for long-wavelength QC lasers (e.g. $\Delta E_c{}^L$ well above 100 meV and ΔE_c of at least a few tens meV) can be obtained in Ge/SiGe QWs of the appropriate barrier and substrate compositions. In fact, the values used in this work are quite conservative in this respect, and larger offsets are inferred from the results of some of these studies (most notably Refs. 18 and 24).

III. GAIN-MEDIUM DESIGN MODEL

To design QC gain media based on the material system just described, the effective-mass Schrödinger equation is first solved to compute the energies E and envelope functions $F(\mathbf{r})$ of the L- and Δ-valley bound states. Given the ellipsoidal shape of the constant-energy surfaces of these conduction-band minima, the resulting eigenvalue problem must be written in terms of the inverse effective-mass tensor $\overleftrightarrow{\mathbf{W}}$, as follows:

$$-\frac{\hbar^2}{2}\nabla\cdot\overleftrightarrow{\mathbf{W}}\cdot\nabla F(\mathbf{r})+E_c(z)F(\mathbf{r})=EF(\mathbf{r}), \tag{7}$$

where $E_c(z)$ is the conduction-band lineup computed as discussed in the previous section. Using the Stern-Howard transformation,[26]

$$F(\mathbf{r})=f(z)e^{-i[(k_xW_{xz}+k_yW_{yz})/W_{zz}]z}e^{i(k_xx+k_yy)}, \tag{8}$$

Eq. (7) becomes

$$-\frac{\hbar^2}{2/W_{zz}}f(z)+E_c(z)f(z)=\varepsilon f(z), \tag{9}$$

where the solutions for ε give the subband minima, and the associated in-plane dispersion is

$$E=\varepsilon+\frac{\hbar^2}{2}\left[\left(W_{xx}-\frac{W_{xz}^2}{W_{zz}}\right)k_x^2+\left(W_{xy}-\frac{W_{xz}W_{yz}}{W_{zz}}\right)k_xk_y+\left(W_{yy}-\frac{W_{yz}^2}{W_{zz}}\right)k_y^2\right]. \tag{10}$$

For each L valley the constant-energy ellipsoids are tilted with respect to the (001) growth direction; correspondingly the inverse effective-mass tensor $\overleftrightarrow{\mathbf{W}}$ of Eq. (7) is nondiagonal and can be computed via a unitary transformation from the valley principal coordinate system to the present system where z is along the growth axis. By further choosing the y axis to be perpendicular to the major axis of the ellipsoid under consideration,[27] one finds

$$\overleftrightarrow{\mathbf{W}}^L=\begin{bmatrix}\frac{1}{3}\left(\frac{1}{m_t^L}+\frac{2}{m_l^L}\right) & 0 & \frac{\sqrt{2}}{3}\left(\frac{1}{m_t^L}-\frac{1}{m_l^L}\right)\\ 0 & \frac{1}{m_t^L} & 0\\ \frac{\sqrt{2}}{3}\left(\frac{1}{m_t^L}-\frac{1}{m_l^L}\right) & 0 & \frac{1}{3}\left(\frac{2}{m_t^L}+\frac{1}{m_l^L}\right)\end{bmatrix}, \tag{11}$$

where $m_{l(t)}^L$ is the L-valley longitudinal (transverse) effective mass in the principle coordinate system. On the other hand for each Δ valley $\overleftrightarrow{\mathbf{W}}$ is diagonal with nonzero elements m_l^Δ and m_t^Δ.

The conduction-subband structure of each QC gain-medium design is computed by solving Eq. (9) numerically with a transfer matrix technique. From the resulting energy levels and envelope functions we then evaluate the key laser design parameters, namely, the oscillator strength of the optical transition and the nonradiative ISB relaxation lifetimes. When anisotropic conduction-band minima are involved, as in the present case, the ISB oscillator strength can be written as[28]

$$f=\left\langle\frac{2|\langle l|p_z|u\rangle|^2}{m_0(E_u-E_l)}|\hat{\mathbf{e}}\cdot\overleftrightarrow{\mathbf{W}}\cdot\hat{\mathbf{z}}|^2\right\rangle_{\text{avg}}, \tag{12}$$

where u and l denote the upper and lower laser states, respectively, $\mathbf{p}$ is the momentum operator, $\hat{\mathbf{e}}$ is the polarization

Downloaded 06 Nov 2007 to 128.197.173.60. Redistribution subject to AIP license or copyright, see http://jap.aip.org/jap/copyright.jsp

unit vector of the optical wave, and $\langle\ \rangle_{\rm avg}$ indicates averaging over all equivalent band minima. Thus the L-valley ISB oscillator strength for TM polarized light (i.e., for $\hat{\mathbf{e}}=\hat{\mathbf{z}}$) is inversely proportional to the square of the diagonal effective mass $\langle m_{zz}^L\rangle_{\rm avg}\equiv 1/W_{zz}^L$, which is given by $[2/(3m_t^L)+1/(3m_l^L)]^{-1}$ according to Eq. (11). Using $m_t^L=0.08m_0$ and $m_l^L=1.59m_0$ for Ge (Ref. 11) we obtain $\langle m_{zz}^L\rangle_{\rm avg}=0.12m_0$, which is between two and three times smaller than the estimated effective mass of the heavy holes used in the SiGe ISB emitters reported to date.[8–10] Thus the QC gain media described in this work can be expected to have significantly larger oscillator strengths and hence larger gain coefficients.

Furthermore, according to Eq. (12) the oscillator strength is nonzero even for TE light (i.e., for $\hat{\mathbf{e}}=\hat{\mathbf{x}}$ or $\hat{\mathbf{y}}$), unlike the case of ISB transitions near the Γ minimum of typical III-V QWs. This is due to the coupling between in-plane polarized light and the ISB electric dipoles (which are always orientated along the growth direction in QWs) brought about by the nonzero off-diagonal terms of the inverse effective-mass tensor $\overleftrightarrow{\mathbf{W}}^L$. In particular, using Eqs. (11) and (12) we find that the TE oscillator strength averaged over all the L valleys is inversely proportional to the square of $\langle m_{xz}^L\rangle_{\rm avg}\equiv\sqrt{2}/W_{xz}^L=[1/(3m_t^L)-1/(3m_l^L)]^{-1}$. This off-diagonal effective mass is computed to be about $0.26m_0$ in Ge, which is also small enough to produce substantial optical gain. Thus, unlike traditional III-V QC lasers, the ISB gain media described in this work can emit radiation along the surface normal thereby enabling vertical-cavity laser configurations. This feature may allow overcoming an important limitation of current in-plane terahertz QC lasers, i.e., low outcoupling efficiency and large beam divergence, without resorting to complicated device geometries such as second-order gratings.[29,30]

Besides the oscillator strengths, the other key design parameters of QC gain media are the nonradiative ISB relaxation lifetimes. In the relatively low-doped nonpolar materials under consideration these lifetimes can be expected to be dominated by deformation-potential scattering with nonpolar optical and acoustic phonons.[12] The resulting intravalley scattering rates between two subbands $|i\rangle$ and $|f\rangle$ due to emission (upper sign) and absorption (lower sign) of optical and acoustic phonons can be written as follows:[31]

$$\frac{1}{\tau_{\rm opt}^{\pm}}=\frac{D_0^2 m^* G}{4\pi\hbar^2\rho\omega_0}\left[n(\omega_0)+\frac{1}{2}\pm\frac{1}{2}\right]H(E_i-E_f\mp\hbar\omega_0), \tag{13}$$

$$\frac{1}{\tau_{\rm ac}^{\pm}}=\frac{\Xi^2 k_B T m^* G}{4\pi\hbar^3\rho v_s^2}H(E_i-E_f). \tag{14}$$

In these equations D_0 and Ξ are the scalar optical and acoustic deformation potentials, ω_0 and $n(\omega_0)$ are the $\mathbf{q}=0$ optical phonon frequency and equilibrium number, m^* is the two dimensional (2D) density-of-states effective mass, ρ is the mass density, v_s is the sound velocity, H is the step function, and G is the overlap factor $G=\int dq_z|\langle f|e^{iq_z z}|i\rangle|^2$. Intervalley scattering (L to Δ and L to L) is also important in this context and is treated with a phenomenological model based on an effective deformation potential that includes the contributions of both optical and acoustic phonons.[32,33] In particular, an expression identical to Eq. (13) is used to compute the intervalley scattering rates into each $\Delta(L)$ valley with D_0 and ω_0 replaced by model parameters $D_{L\Delta}$ and $\omega_{L\Delta}$ (D_{LL} and ω_{LL}) extrapolated from experimental data.

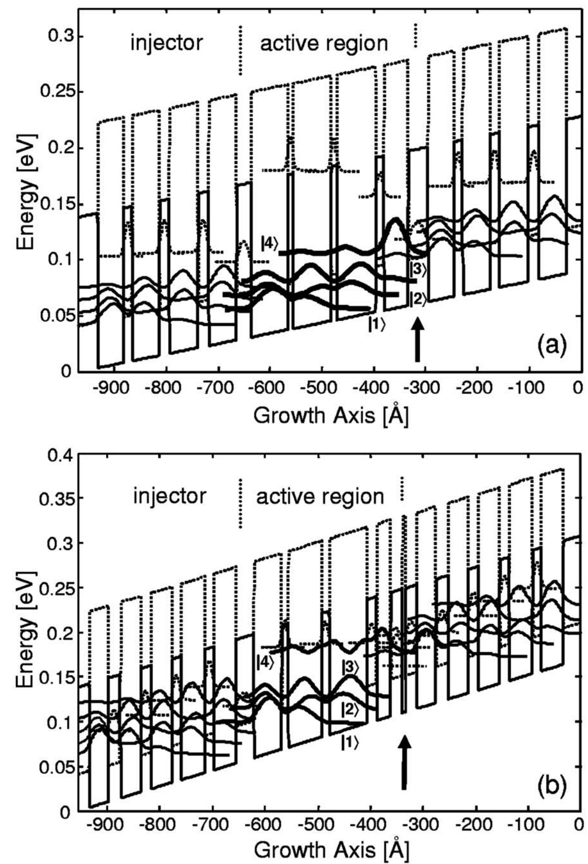

FIG. 4. Conduction-band lineup and squared envelope functions of the relevant bound states of two $Ge/Si_{0.22}Ge_{0.78}$ QC lasers designed for emission near (a) 50 μm and (b) 25 μm. The solid and dotted lines correspond to the L and $\Delta 2$ valleys, respectively. The arrows denote the injection barriers. The horizontal dotted line across the injection barrier in (b) indicates the energy that the local $\Delta 2$ ground state would have if the ultrathin Ge layer were not included in the middle of this "barrier."

To evaluate the lifetimes of Eqs. (13) and (14), we have used material parameters of bulk Ge as appropriate to the high Ge content of the QWs under study. Following Refs. 11 and 32 these parameters are $D_0=3.5\times10^8$ eV/cm, $\Xi=2.5$ eV, $\hbar\omega_0=37$ meV, $\rho=5.32$ g/cm^3, $v_s=3.9\times10^5$ cm/s, $D_{LL}=5.26\times10^8$ eV/cm, $D_{L\Delta 2}=4.65\times10^8$ eV/cm, $\hbar\omega_{LL}=24$ meV, and $\hbar\omega_{L\Delta 2}=23$ meV. Finally, the 2D density-of-states effective mass of the L valleys m_L^* is computed by averaging the dispersion relation of Eq. (10) over all directions on the x-y plane; in conjunction with Eq. (11) this gives $m_L^*=m_t^L(2m_l^L+m_t^L)/(m_l^L+2m_t^L)=0.15m_0$. For the $\Delta 2$ valleys $m_{\Delta 2}^*=m_t^{\Delta}=0.19m_0$.

IV. RESULTS AND DISCUSSION

Shown in Figs. 4(a) and 4(b) are the gain media of two exemplary QC lasers based on the material system of Fig. 3 [i.e., $Ge/Si_{0.22}Ge_{0.78}$ QWs on a $Si_{0.12}Ge_{0.88}$ (001) template], designed for emission near 50 μm (6 THz) and 25 μm (12 THz), respectively. These wavelengths roughly delimit

Downloaded 06 Nov 2007 to 128.197.173.60. Redistribution subject to AIP license or copyright, see http://jap.aip.org/jap/copyright.jsp

the existing gap in the spectral range covered by III-V QC lasers, so that the structures of Fig. 4 are meant to illustrate the potential of the Ge/SiGe material system to close out this gap.[34] In these plots the solid (dotted) lines give the conduction-band lineup and squared envelope functions of the relevant bound states in the L ($\Delta 2$) valleys. Starting from the injection barrier, indicated by the arrow in each figure, and proceeding downstream the layer thicknesses for a single stage are **38**/47/**15**/76/**10**/74/**9**/72/**28**/54/**20**/56/**18**/53/**17**/50 Å for the 50 μm design of Fig. 4(a) and **22**/6/**22**/26/**19**/71/**15**/63/**13**/53/**34**/42/**17**/44/**18**/40/**20**/38/**23**/36 Å for the 25 μm design of Fig. 4(b) (the bold numbers refer to the SiGe barriers); the externally applied electric fields are 9.8 and 19.0 kV/cm, respectively. Both structures employ the bound-to-continuum scheme with a four-well active region and a chirped injector. Light emission involves electronic transitions between the L-valley states labeled $|4\rangle$ and $|3\rangle$, whose energy differences δE are 24.6 and 50.0 meV in Figs. 4(a) and 4(b), respectively. Rapid depopulation of the lower laser states $|3\rangle$ occurs through phonon-assisted scattering into states $|2\rangle$ and $|1\rangle$. Finally, electrons are recycled from each active region to the next through miniband transport in the injector.

In the development of n-type silicon-based QC structures such as the examples of Fig. 4, two design considerations specific to the Ge/SiGe material system should be kept into account. First, relatively diagonal laser transitions (i.e., involving subbands mainly localized in neighboring QWs) must be employed to satisfy the general condition for population inversion $\tau_{43} > \tau_3$, where $1/\tau_{43}$ is the scattering rate from $|4\rangle$ to $|3\rangle$ and τ_3 is the overall lifetime of $|3\rangle$. In III-V QWs the dominant ISB scattering mechanism is the electron/LO-phonon polar interaction, whose matrix elements are inversely related to the wavevector of the phonon involved and thus depend on the ISB energy separation in a resonant fashion (i.e., the closer the energy separation to the LO-phonon energy, the larger the matrix elements). As a result, in III-V QC lasers the ISB energy separations provide a very effective design parameter to engineer the relevant lifetimes. On the other hand in SiGe alloys such polar interaction is absent, and ISB relaxation is dominated by deformation-potential scattering which does not exhibit any resonant behavior [e.g., see Eqs. (13) and (14)]. Thus the ISB scattering rates can only be controlled through the envelope-function spatial overlaps G, and the condition for population inversion requires that the overlap between the laser subbands $|3\rangle$ and $|4\rangle$ be small relative to that between $|3\rangle$ and its lower-lying subbands $|1\rangle$ and $|2\rangle$. This requirement is satisfied by the diagonal design of Figs. 4(a) and 4(b).

The second specific design consideration is related to the bound $\Delta 2$ states in the SiGe "barriers." Namely, each such state must be surrounded by neighboring L states at lower energy; otherwise intervalley scattering would lead to a trapping and buildup of electrons in the $\Delta 2$ valleys, resulting in inefficient and possibly unstable transport into the laser states. This requirement is particularly critical for the $\Delta 2$ bound states in the injection barriers, as these are typically the thickest barrier layers in high-performance QC structures. Thus one has to ensure that the upper laser states $|4\rangle$ remain at lower energy compared to the $\Delta 2$ bound states in the adjacent injection barriers, a constraint that ultimately limits the shortest achievable emission wavelength with this material system.

A possible approach to mitigate this limitation has been used in the design of the 25 μm device of Fig. 4(b). In this structure an ultrathin (6 Å) Ge layer is inserted in the middle of each injection barrier to push up the local $\Delta 2$ bound states while at the same time maintaining the desired spatial separation between the neighboring upper laser state and injector miniband. To illustrate the effectiveness of this approach, the energy of the injection-barrier $\Delta 2$ ground state in the absence of the ultrathin Ge layer is indicated by the horizontal dotted line in Fig. 4(b), which clearly lies well below the adjacent upper laser state $|4\rangle$. It should be mentioned that this idea has already been experimentally demonstrated with GaAs/AlGaAs QC lasers to minimize the impact of Γ-to-X intervalley scattering, thereby allowing emission at record short wavelengths ($\sim$7 μm) for these devices.[35] An alternative design that does not require especially thick injection barriers is the "superdiagonal" scheme, in which the upper laser subbands are provided by the ground states of the injector minibands;[36,37] however, its implementations with III-V midinfrared devices so far have not reached state-of-the-art performance. Finally, a very recent theoretical study has also suggested that the use of Ge/GeSiSn QWs in similar QC structures would result in $\Delta 2$ band edges at sufficiently high energies so that they no longer affect the quantum confinement in the L valleys.[38] This is also a promising approach, although the development of this QW material system is currently still in its very early stages.

In order to assess the performance of the structures of Fig. 4 we have used a simple rate-equation model of QC lasers,[39] which leads to the following expression for the material gain coefficient:

$$g_{\mathrm{TE,TM}} = \frac{\hbar q^2}{\varepsilon_0 c m_0} \frac{\eta f_{\mathrm{TE,TM}}}{n \gamma L_p} \left[\tau_4 \left(1 - \frac{\tau_3}{\tau_{43}} \right) \frac{J}{q} - N_d e^{-\Delta/k_B T} \right]. \tag{15}$$

Here η is the injection efficiency, $f_{\mathrm{TE,TM}}$ is the oscillator strength of Eq. (12), n is the refractive index, γ is the full width at half maximum (FWHM) of the laser transition, L_p is the length of one period of the active material, J is the injected current density, N_d is the donor sheet density per period, and Δ is the energy separation between each lower laser state and the quasi-Fermi level of the injector downstream.

Shown in Fig. 5 is the calculated TM differential gain dg_{TM}/dJ plotted versus temperature for the structures of Fig. 4(a) (solid line) and 4(b) (dashed line); for TE light these curves should be rescaled by the factor $f_{\mathrm{TE}}/f_{\mathrm{TM}}$, given by $\langle m_{zz}^L \rangle_{\mathrm{avg}}^2 / \langle m_{xz}^L \rangle_{\mathrm{avg}}^2 = 0.21$ according to Eq. (12). In these simulations we assumed a typical donor sheet density for long-wavelength QC lasers $N_d = 5 \times 10^{10}$ cm^{-2}, unit injection efficiency $\eta = 1$, and a conservative value for the FWHM of the lasing transitions $\gamma/\delta E = 25\%$.[8–10] The lifetimes τ_4, τ_3, and τ_{43} were computed using Eqs. (13) and (14) and including scattering into all neighboring subbands in all valleys. Exemplary values for the 50 μm structure of Fig. 4(a) at room

Downloaded 06 Nov 2007 to 128.197.173.60. Redistribution subject to AIP license or copyright, see http://jap.aip.org/jap/copyright.jsp

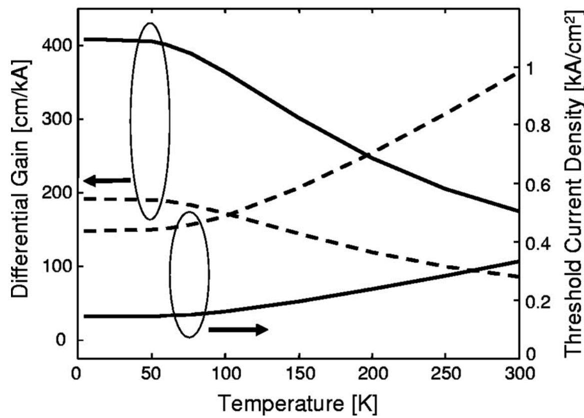

FIG. 5. Calculated TM differential gain coefficient dg_{TM}/dJ and threshold current density J_{th} for the QC lasers of Fig. 4(a) (solid) and 4(b) (dashed).

temperature are $\tau_3=8.1$ ps, $\tau_4=11.3$ ps, and $\tau_{43}=30.3$ ps, which are larger than the nonradiative lifetimes of typical III-V QC lasers by an order of magnitude. The resulting relatively large values of dg_{TM}/dJ shown in Fig. 5 indicate that low-threshold laser operation can be expected from these gain media when combined with properly designed optical cavities. To illustrate, in Fig. 5 we also plot the corresponding threshold current densities J_{th} for TM light computed from the laser gain condition $\Gamma g_{\mathrm{TM}}(J_{\mathrm{th}})=\alpha_m+\alpha_w$. The waveguide loss coefficient α_w and confinement factor Γ were taken from recent simulations of SiGe surface plasmon waveguides at similar wavelengths,[40] giving $\alpha_w=10$ (40) cm^{-1} and $\Gamma=35$ (60)% for the device emitting at 50 (25) μm; for the mirror loss coefficient α_m, a value of 10 cm^{-1} was used as appropriate to a typical cavity length of 1 mm.

The threshold current densities of a few hundred $\mathrm{A/cm}^2$ plotted in Fig. 5 compare favorably with those of existing III-V far-infrared QC lasers. These results therefore indicate that high-performance Ge/SiGe lasers can indeed be designed for emission over a broad spectral range, including wavelengths that are not readily accessible with III-V devices. The ability to provide room-temperature operation is also suggested in Fig. 5; however, an accurate estimate of the highest achievable operating temperature likely requires a more detailed theoretical model, including electron-electron scattering processes and hot-carrier effects. Such models of QC lasers have been developed recently[41,42] but are quite demanding from a computational viewpoint, and their extension to the present devices is beyond the scope of this article. For this reason we also did not consider QC gain media with emission photon energies below all the relevant optical phonon energies, in which electron-electron scattering can be expected to provide the dominant contribution to the inter-laser-subband lifetime τ_{43} at least at low temperatures. In any case, we note that the comparatively long phonon scattering lifetimes of SiGe QWs are still very favorable to maintain a population inversion at high temperatures, especially in bound-to-continuum structures such as the examples of Fig. 4 where the lower laser subbands are also efficiently depopulated via electron-electron scattering.[41]

V. CONCLUSIONS

In summary we have presented a detailed account of the design of terahertz QC lasers based on electronic ISB transitions in Ge/SiGe QWs grown on SiGe (001) templates. The model-solid theory of band offsets has been applied to investigate the achievable quantum confinement in these heterostructures and to identify optimal barrier and template alloy compositions. With this procedure we have shown that the Ge L-valley electrons can be confined in sufficiently deep potential wells for the development of far-infrared QC lasers, particularly if the SiGe barriers are thin enough to effectively suppress L-to-$\Delta 2$ intervalley scattering. Two Ge/SiGe QC gain media have then been designed and modeled, using the effective-mass Schrödinger equation for the L and $\Delta 2$ valleys and standard expressions for the electron-phonon scattering lifetimes. Due to the nonpolar nature of SiGe and the resulting lack of reststrahlen absorption and of resonant electron-phonon scattering, this class of QC lasers can extend the spectral range covered by III-V materials, as illustrated with the choice of emission wavelengths for the two designed structures (near 25 and 50 μm). The absence of polar electron/LO-phonon interactions, which typically dominate ISB relaxation in III-V QWs, also results in relatively long nonradiative lifetimes, and hence large optical gain coefficients and potential for high-temperature operation. Additionally, the tensor properties of the L-valley effective mass allow for significant TE gain, which is desirable for the development of vertically emitting ISB lasers. The devices presented in this work are therefore very promising for high-performance operation across the terahertz spectral region, with the additional advantage of full compatibility with the silicon microelectronics platform.

[1] M. Lee and M. C. Wanke, Science **316**, 64 (2007).
[2] R. Köhler, A. Tredicucci, F. Beltram, H. E. Beere, E. H. Linfield, A. G. Davies, D. A. Ritchie, R. C. Iotti, and F. Rossi, Nature (London) **417**, 156 (2002).
[3] G. Scalari, L. Ajili, J. Faist, H. E. Beere, E. H. Linfield, D. A. Ritchie, and A. G. Davies, Appl. Phys. Lett. **82**, 3165 (2003).
[4] B. S. Williams, H. Callebaut, S. Kumar, Q. Hu, and J. L. Reno, Appl. Phys. Lett. **82**, 1015 (2003).
[5] H. Luo, S. R. Laframboise, Z. R. Wasilewski, G. C. Aers, H. C. Liu, and J. C. Cao, Appl. Phys. Lett. **90**, 041112 (2007).
[6] G. Sun, L. Friedman, and R. A. Soref, Appl. Phys. Lett. **66**, 3425 (1995).
[7] L. Friedman, R. A. Soref, and G. Sun, J. Appl. Phys. **83**, 3480 (1998).
[8] G. Dehlinger, L. Diehl, U. Gennser, H. Sigg, J. Faist, K. Ensslin, D. Grützmacher, and E. Müller, Science **290**, 2277 (2000).
[9] I. Bormann, K. Brunner, S. Hackenbuchner, G. Zandler, G. Abstreiter, S. Schmult, and W. Wegscheider, Appl. Phys. Lett. **80**, 2260 (2002).
[10] S. A. Lynch, R. Bates, D. J. Paul, D. J. Norris, A. G. Cullis, Z. Ikonić, R. W. Kelsall, P. Harrison, D. D. Arnone, and C. R. Pidgeon, Appl. Phys. Lett. **81**, 1543 (2002).
[11] F. Schäffler, Semicond. Sci. Technol. **12**, 1515 (1997).
[12] K. Reimann, R. A. Kaindl, and M. Woerner, Phys. Rev. B **65**, 045302 (2001).
[13] K. Driscoll and R. Paiella, Appl. Phys. Lett. **89**, 191110 (2006).
[14] R. Braunstein, A. R. Moore, and F. Herman, Phys. Rev. **109**, 695 (1958).
[15] J. Weber and M. I. Alonso, Phys. Rev. B **40**, 5683 (1989).
[16] C. G. Van de Walle and R. M. Martin, Phys. Rev. B **34**, 5621 (1986).
[17] L. Colombo, R. Resta, and S. Baroni, Phys. Rev. B **44**, 5572 (1991).
[18] M. M. Rieger and P. Vogl, Phys. Rev. B **48**, 14276 (1993).
[19] G. P. Schwartz, M. S. Hybertsen, J. Bevk, R. G. Nuzzo, J. P. Mannaerts, and G. J. Gualtieri, Phys. Rev. B **39**, 1235 (1989).
[20] E. T. Yu, E. T. Croke, T. C. McGill, and R. H. Miles, Appl. Phys. Lett. **56**, 569 (1990).

Downloaded 06 Nov 2007 to 128.197.173.60. Redistribution subject to AIP license or copyright, see http://jap.aip.org/jap/copyright.jsp

[21]L. Yang, J. R. Watling, R. C. W. Wilkins, M. Borici, J. R. Barker, A. Asenov, and S. Roy, Semicond. Sci. Technol. **19**, 1174 (2004).
[22]Y.-H. Kuo, Y. K. Lee, Y. Ge, S. Ren, J. E. Roth, T. I. Kamins, D. A. B. Miller, and J. S. Harris, Nature (London) **437**, 1334 (2005).
[23]S. Tsujino, H. Sigg, G. Mussler, D. Chrastina, and H. Von Känel, Appl. Phys. Lett. **89**, 262119 (2006).
[24]M. Virgilio and G. Grosso, J. Phys.: Condens. Matter **18**, 1021 (2006).
[25]S. Galdin, P. Dollfus, V. Aubry-Fortuna, P. Hesto, and H. J. Osten, Semicond. Sci. Technol. **15**, 565 (2000).
[26]F. Stern and W. E. Howard, Phys. Rev. **163**, 816 (1967).
[27]W. Xu, Y. Fu, and M. Willander, Phys. Rev. B **49**, 13760 (1994).
[28]S. K. Chun and K. L. Wang, Phys. Rev. B **46**, 7682 (1992).
[29]O. Demichel, L. Mahler, T. Losco, C. Mauro, R. Green, J. H. Xu, A. Tredicucci, F. Beltram, H. E. Beere, D. A. Ritchie, and V. Tamosiunas, Opt. Express **14**, 5335 (2006).
[30]J. A. Fan, M. A. Belkin, F. Capasso, S. Khanna, M. Lachab, A. G. Davies, and E. H. Linfield, Opt. Express **14**, 11672 (2006).
[31]B. K. Ridley, *Electrons and Phonons in Semiconductor Multilayers* (Cambridge University Press, Cambridge, 1997), Chap. 1.
[32]M. V. Fischetti, IEEE Trans. Electron Devices **38**, 634 (1991).
[33]J. Singh, *Electronic and Optoelectronic Properties of Semiconductor Structures* (Cambridge University Press, Cambridge, 2003), Chap. 6.
[34]It should be noted, however, that a few absorption features related to multiphonon processes are observed in the far-infrared transmission spectrum of Ge, most notably near 30 μm [e.g. see J. E. Peters and P. D. Ownby, Opt. Eng. **38**, 1924 (1999)]. Thus, devices emitting in the spectral vicinity of these features can be expected to suffer from higher internal losses.
[35]L. R. Wilson, D. A. Carder, J. W. Cockburn, R. P. Green, D. G. Revin, M. J. Steer, M. Hopkinson, G. Hill, and R. Airey, Appl. Phys. Lett. **81**, 1378 (2002).
[36]J. Faist, F. Capasso, C. Sirtori, D. L. Sivco, A. L. Hutchinson, and A. Y. Cho, Nature (London) **387**, 777 (1997).
[37]S. Blaser, L. Diehl, M. Beck, J. Faist, U. Oesterle, J. Xu, S. Barbieri, and F. Beltram, IEEE J. Quantum Electron. **37**, 448 (2001).
[38]G. Sun, H. H. Cheng, J. Menéndez, J. B. Khurgin, and R. A. Soref, Appl. Phys. Lett. **90**, 251105 (2007).
[39]C. Sirtori and R. Teissier, in *Intersubband Transitions in Quantum Structures*, edited by R. Paiella (McGraw-Hill, New York, 2006), Chap. 1.
[40]Z. Ikonić, R. W. Kelsall, and P. Harrison, Semicond. Sci. Technol. **19**, 76 (2004).
[41]R. Köhler, R. C. Iotti, A. Tredicucci, and F. Rossi, Appl. Phys. Lett. **79**, 3920 (2001).
[42]D. Indjin, P. Harrison, R. W. Kelsall, and Z. Ikonić, Appl. Phys. Lett. **82**, 1347 (2003).

Downloaded 06 Nov 2007 to 128.197.173.60. Redistribution subject to AIP license or copyright, see http://jap.aip.org/jap/copyright.jsp